Deposition mechanism of nanostructured thin films from tetrafluoroethylene glow discharges*

A. Milella[1,‡], F. Palumbo[2], P. Favia[1], G. Cicala[2], and R. d'Agostino[1]

[1]*Dipartimento di Chimica, Università degli Studi di Bari, via Orabona 4, 70126 Bari, Italy;* [2]*Istituto di Metodologie Inorganiche e dei Plasmi, CNR-IMIP, via Orabona 4, 70126 Bari, Italy*

Abstract: Nanostructured polytetrafluoroethylene (PTFE)-like thin films can be deposited, in certain experimental conditions, by modulated discharges fed with tetrafluoroethylene (TFE). These coatings are characterized by a unique morphology consisting of highly twisted micron-long ribbons, which leads to an extremely high water repellency of the surface. In the present work, the diagnostics of the plasma phase is presented, coupled with that of the coating, in order to understand the film growth mechanism in different discharge regimes. When the duty cycle (DC) is increased in modulated C_2F_4 plasmas, the monomer depletion increases, too, and many recombination reactions take place at progressively higher rates, resulting in the formation of CF_4, C_2F_6, C_3F_6, C_3F_8, and C_4F_{10}; the formation of powders in the homogeneous phase, however, was never evidenced. The modulation of C_2F_4 plasmas strongly affects the morphology of the resulting coating, as revealed by atomic force microscopy (AFM), ranging from bumpy to ribbon-like structures. The latter, moreover, are found to be more PTFE-like with respect to the remaining part of the film. In the last part of the paper, a deposition mechanism is proposed, where low radical densities in the plasma and surface migration of the precursors are the keys for the growth of ribbon-like structures.

Keywords: PECVD; gas-phase diagnostics; fluorocarbon coatings; nanostructures.

INTRODUCTION

Conventional polytetrafluoroethylene (PTFE) is characterized by many remarkable properties such as a low dynamic friction coefficient, high thermal stability, low dielectric constant, low critical surface tension, and extremely high chemical resistance [1], which make this material potentially suitable for many technological fields, from textiles [2] to biomaterials [3–10], as well as in microelectronics [11–16].

Over the years, the development of gas-phase techniques for the deposition of PTFE-like films with a stoichiometry as close as possible to that of bulk PTFE [12–30] has been extensively investigated. As regards plasma-enhanced chemical vapor deposition (PECVD), very good control over film chemical composition is obtained by using modulated plasmas. In modulated plasmas, the discharge is periodically switched on (on time, t_{on}) and off (off time, t_{off}). The duty cycle (DC), which is the percent of time the discharge is on, and the period ($t_{on} + t_{off}$) proved to be key parameters in tuning film chemical composition and structure. More specifically, several authors found that lowering the DC in modulated plasmas results in a progressively less branched film structure, and in an increased retention

---

‡Corresponding author: E-mail: milella@chimica.uniba.it

of monomer structure in the coating [12,31–37]. This result can be explained by a reduced extent of fragmentation of the monomer in the gas phase and a less energetic ion bombardment at the growing film surface during the on time. Ion bombardment, in fact, usually leads to structural rearrangement, cross-linking, etching, or defluorination of the film, resulting in a more damaged polymer surface. Fluorocarbon films with compositions very close to bulk PTFE were deposited from modulated discharges fed with hexafluoropropylene oxide (HFPO), with F/C ratios as high as 1.8–1.9 [33,36].

Lately, several studies have been devoted to the tailoring of film morphology, in addition to film chemical composition, as a way to control film properties [14,38–41]. Superimposing a controlled surface roughness with a tunable chemical composition results in an additional tool for modulating hydrophobicity of the deposited fluorocarbon coating, eventually reaching ultra-hydrophobic character, as predicted by the Wenzel equation [42]. In the literature, several strategies have been described to obtain water-repellent surfaces. Washo reported contact angles of 165°–170° for plasma-polymerized PTFE films deposited in the powder formation region [38]. Other techniques include two-step processes, the first one being a roughening procedure [39–41]. On the other hand, single-step deposition of fluorocarbon films by modulated discharges fed with alkene precursors containing long perfluoroalkyl chains, is described in ref. [34] and a maximum contact angle value of 130° was found.

In previous publications [43–45], we reported single-step deposition of ultra-hydrophobic fluorocarbon films from modulated tetrafluoroethylene (TFE) discharges. The ultra-hydrophobic character was therein ascribed to the unique film morphology, consisting of a surface structured with ribbon-shaped micro-/nanostructures. The deposition of such kinds of coatings occurs only under selected modulation conditions, namely, low DCs ($\leq$7 %) and long periods ($\geq$200 ms).

In this paper, we report our recent results on C_2F_4-modulated glow discharges, where the plasma phase is investigated using Fourier transform infrared absorption spectroscopy (FT-IRAS), and the morphology of films prepared under different discharge conditions is studied by atomic force microscopy (AFM). Moreover, some results on film chemical composition as determined by imaging time-of-flight secondary ion mass spectrometry (ToF-SIMS) investigations will be also described. Finally, the present results are combined with previous ones for proposing a film growth mechanism.

EXPERIMENTAL

The coatings were deposited in a parallel plate stainless steel reactor, described in detail elsewhere [46]. The upper powered electrode (12-cm stainless steel disk) and the lower grounded (19-cm stainless steel disk) are spaced 5 cm apart. The plasma is sustained with a 13.56 MHz power supply (RF Power Products, model RF5) equipped with a card that allows modulated operating conditions, by changing the DC and/or the on time. Impedance matching is accomplished with an LC network (Ulvac, model 002A). An oscilloscope (Tektronix, model TDS 200) is used to monitor the pulse duration and amplitude, and a second channel also allows one to monitor the radio frequency (rf) wave. The TFE flow rate and pressure were regulated and controlled by means of electronic mass flow controllers and a capacitive pressure gauge (Baratron MKS Instruments). The system is continuously pumped by a rotary pump, which allows a base pressure of 10^{-3} torr. Polished silicon substrates, placed on the ground electrode, were processed, feeding TFE at 6 sccm and setting the other experimental parameters as listed in Table 1.

Table 1 Experimental parameters.

Power (W)	Pressure (mtorr)	DC (%)	Period (ms)	Deposition time (s)
5–150	100–500	5–100	40–320	25–21 600

The gas-phase diagnostics were carried out through ZnSe windows for FT-IRAS. To inhibit film formation on the optical windows, these were mounted 25 cm away from the interelectrode region and heated to 60 °C by wrapping the flanges with a heating tape.

A commercial FT-IR interferometer (Bruker Equinox 55) equipped with a Globar source was used to collect infrared absorption spectra: a parallel beam traverses the plasma through the ZnSe window and is then focused with a gold-coated paraboloid mirror onto a mercury cadmium telluride (MCT) detector cooled with liquid N_2. A continuous N_2 purge was used during each acquisition to reduce absorption from CO_2 and H_2O. Infrared spectra of the gas phase were recorded from 500 to 7500 cm^{-1} with a spectral resolution of 1 cm^{-1} over 250 scans, when signal assignments were to be carried out. For partial pressure determination, instead, a spectral resolution of 4 cm^{-1} was used, and the spectrum was acquired over an average of 1000 scans. This allows the improvement of the signal-to-noise ratio in order to better quantify less abundant species. In order to obtain the highest possible resolution, a Boxcar apodization function was utilized [47,48], and a reference scan was acquired immediately before each sample scan.

ToF-SIMS was carried out with a CAMECA TOF IV reflectron instrument. A 25 keV $^{69}Ga^+$ primary ion source with an ion current of 1.3 nA was utilized, capable of a mass resolution of 6000. Data were acquired over a m/z range from 0 to 450 for both positive and negative secondary ions, and the area of analysis was 100×100 μm^2. Ion images, 30×30 μm^2 wide, of structured samples were acquired in order to evaluate the ion distribution in the surface region. A flux of low-energy electrons was utilized to minimize sample charging during analyses.

Changes in surface morphology with changing process parameters were assessed by AFM. The AFM images were acquired with a microscope (Thermomicroscopes Autoprobe CP) in the non-contact mode using conical gold-coated silicon high-resonance frequency (280 kHz) probe tips. The non-contact mode was generally the acquisition mode, to prevent possible surface damage owing to continuous tip contact with the sample surface. In some cases, however, both contact- and non-contact images were acquired on the same sample surface, in order to assess the true topography. On each sample, the following areas were analyzed: 50×50 μm^2, 20×20 μm^2, 10×10 μm^2, 5×5 μm^2. The overall appearance of the surface was evaluated from the bigger areas, 50×50 μm^2 and 20×20 μm^2, while the other images were taken into account for a better analysis of surface features. Root mean square roughness (RMS), defined by eq. 1, was evaluated on five different areas of each sample, to verify surface uniformity.

$$\text{RMS} = \sqrt{\frac{1}{N} \sum_{i=1}^{N} \left\langle Z_i - \bar{Z} \right\rangle^2} \tag{1}$$

In eq. 1, N is the total number of points in the AFM image, Z_i is the height of the point i, and $\bar{Z}$ is the average height.

RESULTS

Gas-phase diagnostics

The infrared spectra of plasmas modulated at 5 and 70 % DC, at a fixed modulation period of 320 ms, are shown in Fig. 1. Input power and chamber pressure were fixed at 100 W and 200 mtorr, respectively. The identification of the molecules present in the plasma was based on comparison with the infrared spectra of several fluorocarbon gases recorded in the same reactor with the plasma off. In particular, considering the spectra reported in Fig. 2, it is possible to describe the main features of Fig. 1 as follows. At 1281 cm^{-1}, the main signal of CF_4 and at 1250 cm^{-1} that of C_2F_6, which partially overlap, can be identified. C_2F_6 is confirmed by the band at 1117 cm^{-1}, while the ones at 1337 cm^{-1} and 1186 cm^{-1} are due to the undissociated monomer, C_2F_4. A certain amount of C_3F_8 is also produced in the plasma,
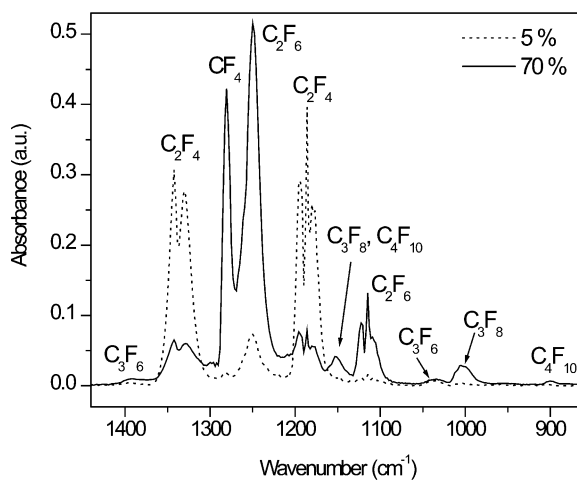
Fig. 1 FT-IR spectra of modulated TFE plasmas at DC of 5 and 70 %. Input power and pressure were fixed at 100 W and 200 mtorr, respectively. Reported spectra were acquired at a resolution of 4 cm^{-1}.
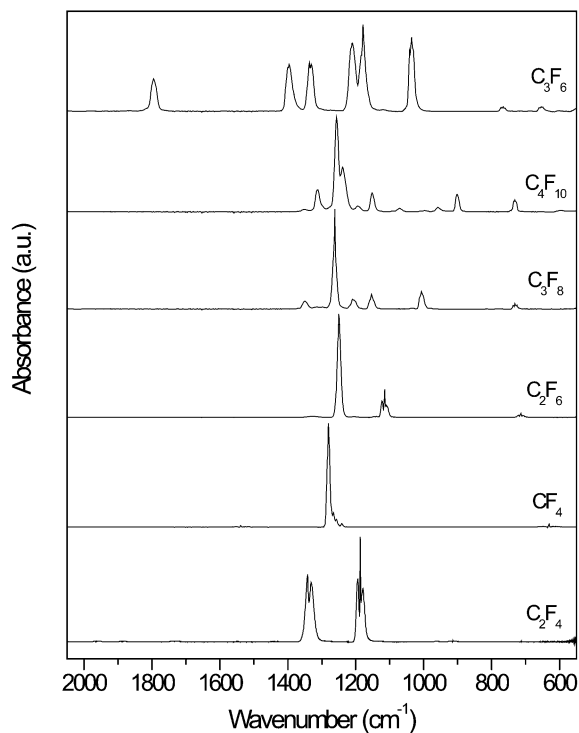

Fig. 2 FT-IR spectra of the fluorocarbon gases identified in TFE continuous and modulated plasmas. Spectra were acquired at a resolution of 1 cm^{-1}.

as indicated by the presence of the weak absorption band at 1004 cm^{-1}. C_3F_8 shows a strong absorption at 1261 cm^{-1}, which is hidden by CF_4 and C_2F_6 absorption bands in the C_2F_4 plasma. The small band at 900 cm^{-1} was assigned to C_4F_{10}, while those at 1396 cm^{-1} and 1037 cm^{-1} can be assigned to C_3F_6, the presence of which is confirmed by a band (not shown) at 1790 cm^{-1}. The production of C_4F_6 and c-C_4F_8 in a C_2F_4 plasma was ruled out since the strongest absorptions bands of these species, at 973 cm^{-1} and 964 cm^{-1}, respectively, were not found.

In order to allow a semi-quantitative analysis of the species produced in the plasma, some calibration curves were used, by following the absorption trends of several bands, for each gas, as a function of the pressure. If the measurements are performed with a limited spectral resolution, the integrated absorption does not depend linearly on the density of the absorbing species, causing an error in the determined density. At high densities, total absorption is a common source of error as well. Therefore, the linearity of the absorption curve as a function of the species density (pressure) has to be checked [47,49]. For all gases considered, the calibration curves show a linear trend in the pressure range investigated (1–500 mtorr). The quantitative approach proposed is possible, provided the gas temperature in the plasma remains the same as discharge parameters are varied. It has been reported elsewhere that both vibrational and rotational temperatures, in fluorocarbon rf discharges operating under experimental conditions similar to those of the present work, are almost equal to ambient temperature [49]. As a validation of this semi-quantitative analysis, the following approach was developed. For each species, the normalized absorbance integrals of different absorption bands were plotted as a function of the DC, and it was found that the curves for each band are close, as shown in Fig. 3. It can be concluded that gas temperature is quite constant in the power range considered, or that it influences the absorption coefficients of these species only slightly. In fact, changes in gas temperature should affect absorption coefficients, leading to different absorption trends. However, it should be considered that the infrared radiation samples both the plasma region and, even more important, a gas volume unaffected by the plasma. Thus, the absorption features represent species likely present in both regions.
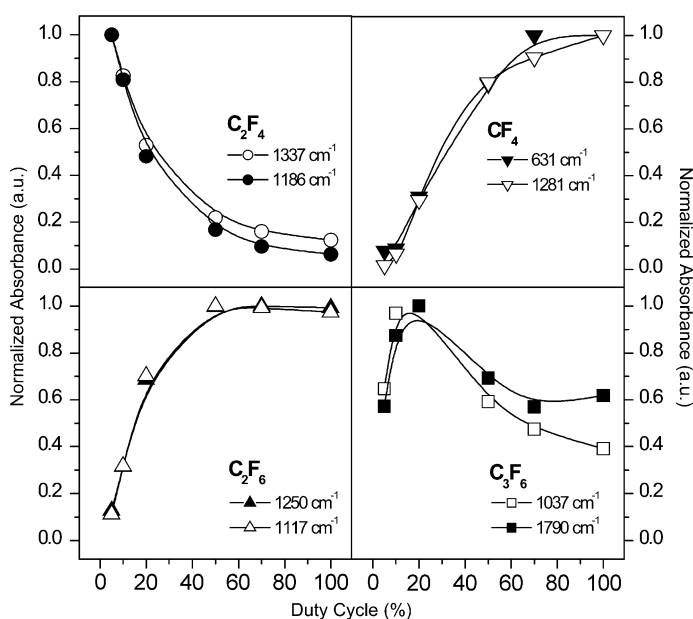

Fig. 3 Effect of DC (at 320 ms of modulation period, 100 W of input power, and 200 mtorr pressure) on the normalized IR integrals of the bands assigned to C_2F_4, CF_4, C_2F_6, and C_3F_6 in TFE-modulated plasma.

As a next step, the partial pressures of all identified species were calculated by using the calibration curves. The absorbance of each species was evaluated by integrating the corresponding band using the same integration type and limits used for the standard gas calibration curves. Figure 4 gathers all curves; for the case of gases with more than one analytical band, the most intense absorption was plotted. It can be stressed that C_2F_4 partial pressure rapidly decreases with a rising DC, but the consumption rate is lower above a DC of 50 %. On the other hand, the concentrations of saturated species rapidly increase and then reach a plateau, though C_3F_8 and C_4F_{10} decrease slightly. C_3F_6, an
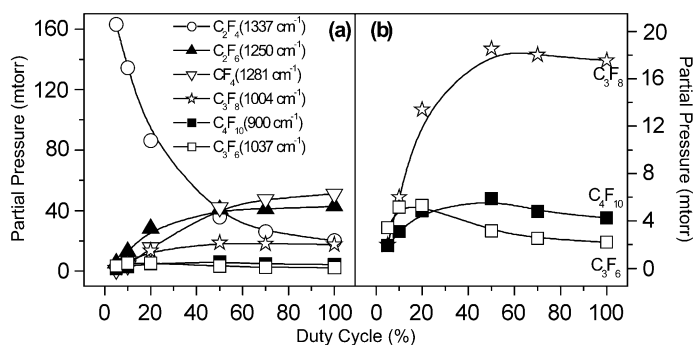
Fig. 4 Effect of the DC on the partial pressures of all the species detected in the plasma (a). The trends of the less abundant species are also reported in (b) for a better visualization.

unsaturated molecule, reaches a maximum and then decreases, most likely due to the high reactivity of the double bond.

This kind of study was also carried out on continuous C_2F_4 plasmas sustained at 200 mtorr and variable input power (5–150 W). Briefly, the same recombination products were detected, with similar trends as well. Moreover, the semi-quantitative analysis revealed that, for each product, the partial pressure at one input power of the continuous discharge is almost the same as that obtained in modulated plasmas at the corresponding average input power, which can be calculated as the DC times the peak power [50,51]. This last result can be explained by the fact that FT-IRAS is not a time-resolved technique.

The appearance of some of the products identified in the plasma was rationalized by some authors [52,53] and can be summarized as follows. The initial decomposition of C_2F_4 leads to the production of $\overset{\bullet}{\underset{\bullet}{C}}F_2$ radicals through the following reaction:

$$CF_2 = CF_2 + e \rightarrow 2\overset{\bullet}{\underset{\bullet}{C}}F_2 + e \tag{2}$$
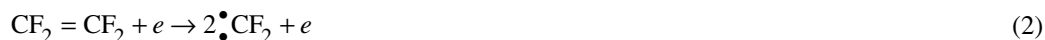
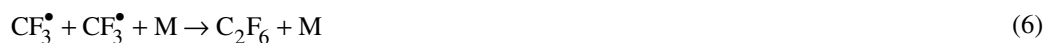Then the following reactions can be taken into account to explain the formation and the loss of C_3F_6 inside the plasma:

$$C_2F_4 + \overset{\bullet}{\underset{\bullet}{C}}F_2 \rightarrow C_3F_6^* \tag{3}$$

$$C_3F_6^* \rightarrow C_3F_6 \tag{4}$$

$$C_3F_6^* \rightarrow CF_3^{\bullet} + CF_2 = CF^{\bullet} \tag{5}$$

where reactions 3 and 5 are overall reactions, which can proceed through several elementary steps.

The formation of C_2F_6 occurs through a recombination of $CF_3^{\bullet}$ radicals:

$$CF_3^{\bullet} + CF_3^{\bullet} + M \rightarrow C_2F_6 + M \tag{6}$$

where M is a third body. The appearance of CF_4 can be explained by considering the following reactions:

$$F^{\bullet} + CF_3^{\bullet} \rightarrow CF_4 \tag{7}$$

Since the C_3F_8 trend is similar to that of CF_4 and C_2F_6, as will be shown later, it could originate from them according to:

$$CF_4 + C_2F_4 \rightarrow C_3F_8 \quad \text{or} \quad CF_4 + \overset{\bullet}{\underset{\bullet}{}}2CF_2 \rightarrow C_3F_8 \tag{8}$$

$$C_2F_6 + {}^{\bullet}_{\bullet}CF_2 \rightarrow C_3F_8 \qquad (9)$$
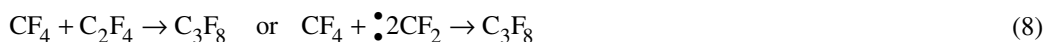
Finally, for the production of C_4F_{10}, the following recombination channels may be proposed:

$$C_3F_8 + {}^{\bullet}_{\bullet}CF_2 \rightarrow C_4F_{10} \qquad (10)$$

$$C_2F_6 + C_2F_4 \rightarrow C_4F_{10} \qquad (11)$$

Also, reactions 8–11 certainly take place through elementary steps eventually induced by electron impact.

FT-IRAS was also used to indicate powder formation inside the plasma, both in the continuous and modulated regimes at different DCs. In fact, scattering of radiation by micron-sized particles in the plasma should lead to a large deviation from the baseline in the absorption spectrum in the range 2000–6000 cm^{-1} [54–56]. In continuous plasmas, no baseline deviation was detected, either by varying the input power in the range 5–150 W at fixed pressure of 200 mtorr, or by changing the pressure from 100 to 500 mtorr at fixed power of 100 W. Analogously, in modulated plasma, no deviation was observed when the DC was varied from 5 to 100 % at 200 mtorr and 100 W, over a deposition time of 90 min. These results allow one to rule out the formation of powders inside the plasma. Nothing more can be said for smaller particulates because of the detection limit of the technique.

Film morphology and composition

A systematic study of the morphology of fluorocarbon films deposited both from continuous and modulated discharges fed with TFE was accomplished by means of AFM.

Figure 5 shows two-dimensional surface topography of the polished silicon substrate and of the films deposited in continuous plasmas at 5, 100, and 150 W, respectively, at a pressure of 200 mtorr. It
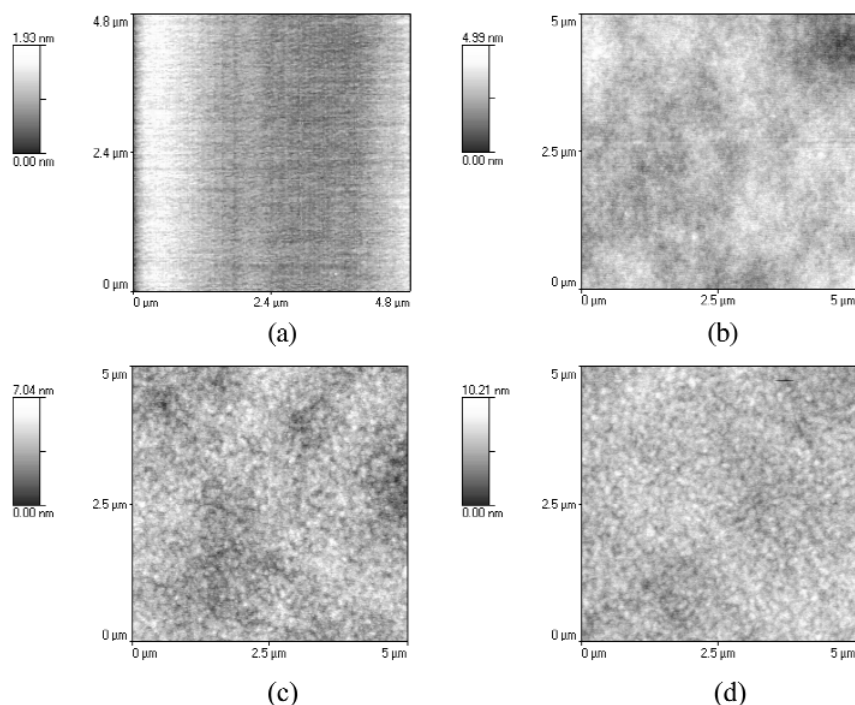

Fig. 5 Two-dimensional AFM topography of polished silicon (a) and of films deposited from TFE continuous plasmas at different input power: 5 W (b), 100 W (c), 150 W (d). Deposition time was 15 min.

is evident that in all conditions the film surface is smooth and that no morphological features can be distinguished. The surface roughness ranges from 0.54 nm for the bare silicon to 1.19 nm for the film deposited at 150 W.

The AFM images of films deposited from continuous discharges at 100 W under varying pressure from 100 to 500 mtorr, are displayed in Fig. 6. At lower pressure the surface is smoother, with a very low value of roughness, 0.87 nm. At 500 mtorr, however, the morphology is characterized by bumps, some of them comprising larger agglomerates. The corresponding roughness increases to 10.94 nm.
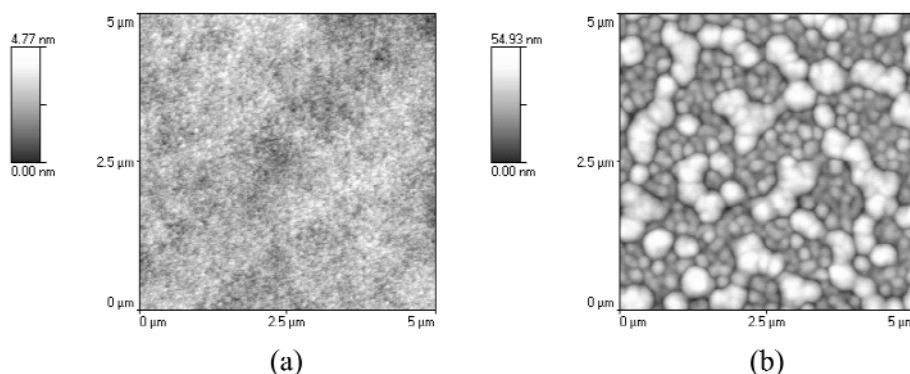

(a)   (b)

Fig. 6 Two-dimensional AFM topography of films deposited from TFE continuous plasmas at 100 mtorr (a) and 500 mtorr (b). Deposition time was 15 min. Input power and gas flow rate were fixed at 100 W and 6 sccm, respectively.

The effect of DC on film morphology at a fixed modulation period of 320 ms and deposition time of 90 min, is shown in Fig. 7. The samples deposited at a DC of 5 % reveal a complex morphology characterized by ribbon-like structures, typically several micrometers long and hundreds of nanometers in width. These ribbons are randomly distributed over the entire surface and twisted in an intricate way. At higher magnification, the image shows that the surface area between these structures is populated by islands of nanometric size, also randomly distributed. Higher magnification allows one to evaluate the diameters of such nuclei as ranging from 80 to 500 nm, with heights varying from 10 to 200 nm. The morphology of the film deposited at a 10 % DC (Fig. 7b) is drastically changed, since no ribbons appear, but only some grains with irregular shape, up to 2 mm long and with a maximum height of about 400 nm. Nuclei are still present, but with a lower spread in heights, from about 2 to 30 nm. The film corresponding to 20 % of DC (Fig. 7c) shows yet another kind of morphology: some larger bumps start to form, align, and coalesce. They exhibit a more regular distribution of diameters, 400 to 600 nm, and heights in the range 70–90 nm. The remaining portion of surface is populated by bumps uniformly dispersed and with very similar diameters of about 200 nm, and maximum height of 20 nm. Further increasing the DC up to 50 % (Fig. 7d) does not change the morphology much over that of its 20 % counterpart. However, in this case, the surface is very rich in bumps, 200 nm wide and with heights close to 10 nm. Moreover, a smaller number of large aggregates with diameters around 400 nm and a maximum height of 30 nm can be observed. Thus, as the DC increases, the height distribution becomes more uniform. At a DC of 70 % (Fig. 7e), the sample is so crowded with bumps that these collapse, lose their individual shape, and lead to a more homogeneous surface. Finally, the continuous-mode deposition (100 % DC, Fig. 7f) results in a flat surface with no evidence of bumps.
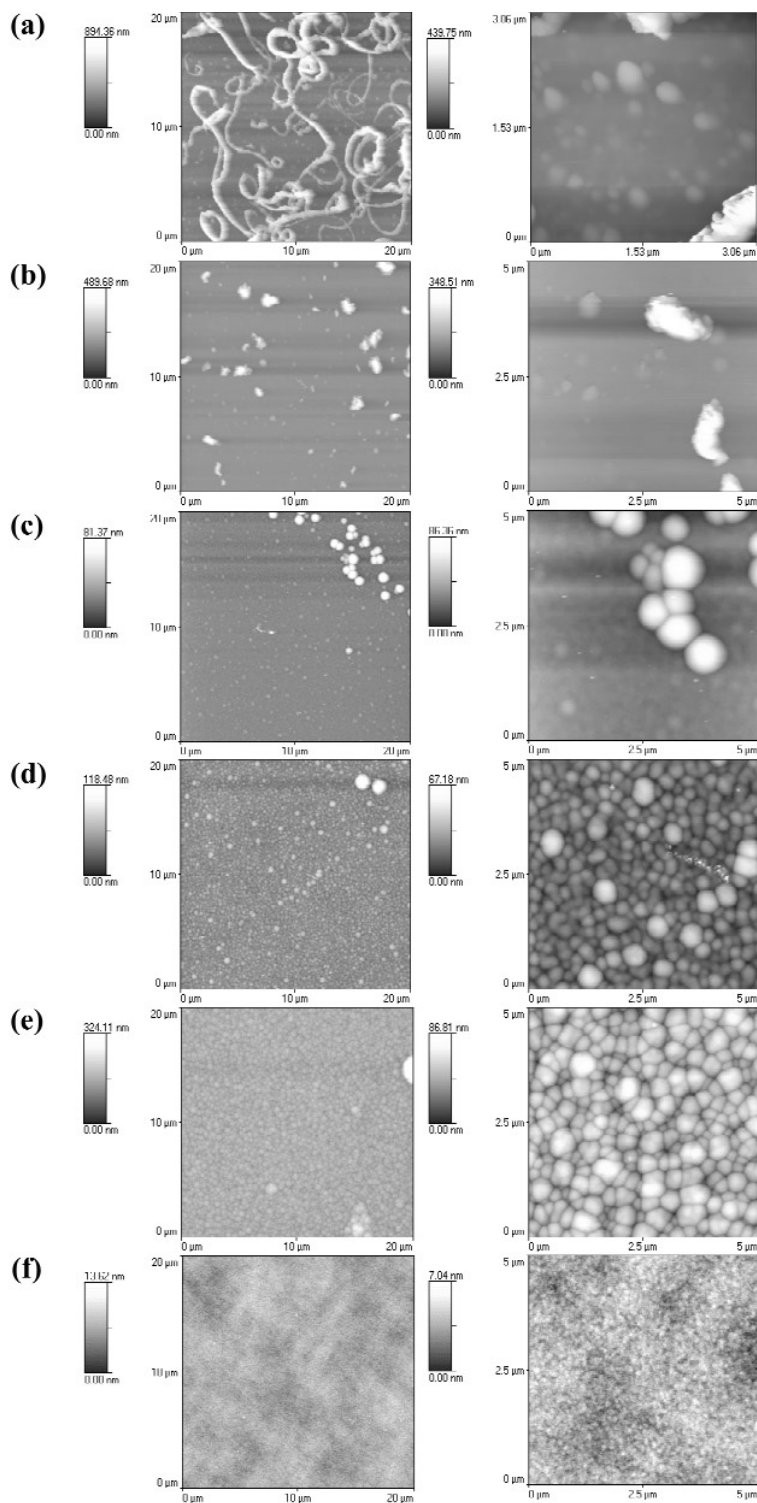
Fig. 7 Non-contact AFM images (20×20 μm^2 and 5×5 μm^2) of films deposited from modulated discharges at 320 ms period with different DCs: 5 % (a), 10 % (b), 20 % (c), 50 % (d), 70 % (e), 100 % (f). Deposition time was 90 min. Input power and pressure were fixed at 100 W and 200 mtorr, respectively.

The effect of the modulation period on the topography of the deposited films is shown in Fig. 8. Even though a DC value of 5 % is used, for a period of 40 ms (Fig. 8a) the process results in a featureless film with very low roughness (2.6 nm). Increasing the period to 80 ms (Fig. 8b) results in very few aggregates becoming visible and the surface roughness becomes 3.2 nm. At a period of 200 ms (Fig. 8c) the sample surface displays aggregates with almost ribbon-like appearance, but shorter than the ones observed at 320 ms (Fig. 8d). Moreover, with respect to the latter, the bumps are reduced in number. The formation of short ribbons results in an increased roughness of 43.9 nm.
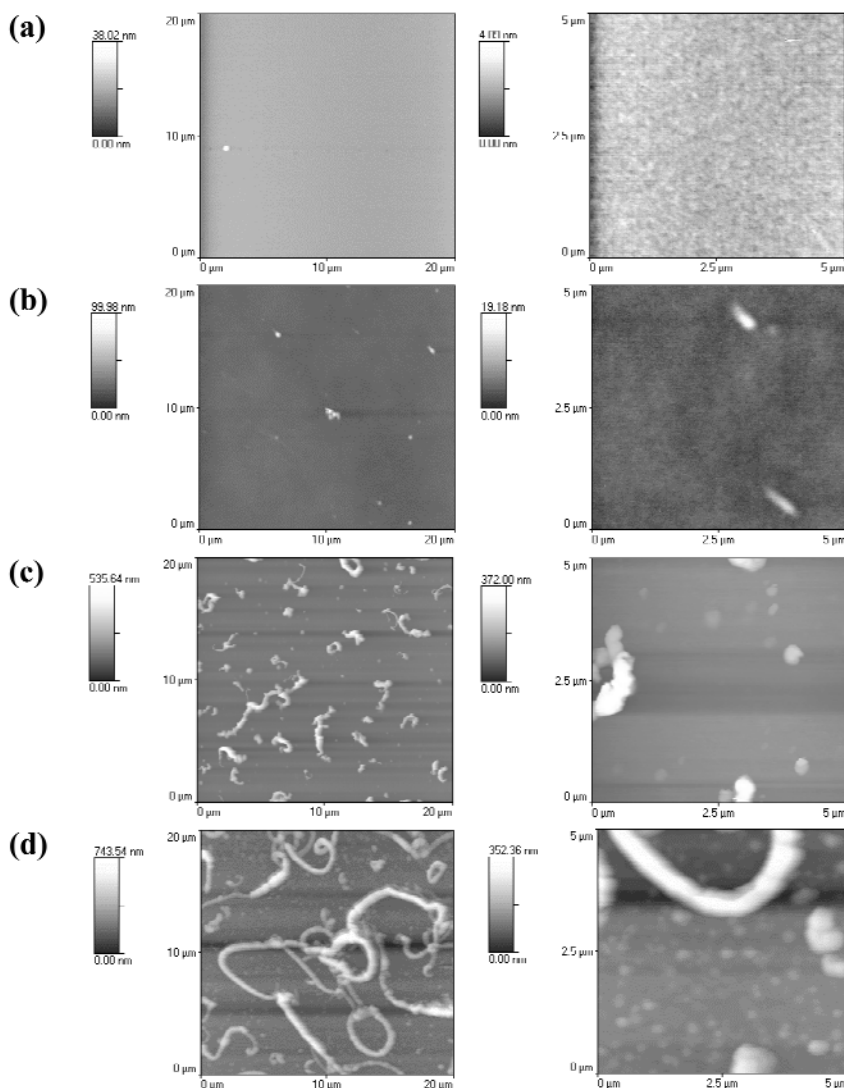

Fig. 8 Non-contact AFM images (20×20 μm^2 and 5×5 μm^2) of films deposited from modulated discharges at 5 % DC with different modulation periods: 40 ms (a), 80 ms (b), 200 ms (c), 320 ms (d). Deposition time was 90 min. Input power and pressure were fixed at 100 W and 200 mtorr, respectively.

Another key parameter for understanding ribbon formation is the deposition time. This effect was thoroughly investigated in previous work [44], in which we basically reported that ribbon formation involves several steps, namely, the formation of nucleation centers at the very first stage of growth, align-

ment, and subsequent attachment of further nuclei for the formation and development of the ribbons. Once the ribbons have grown enough in numbers and dimensions, the formation of further nucleation centers on the ribbon surfaces occurs. The shape and dimensions of the morphological features have been confirmed by SEM analyses (not reported).

ToF-SIMS analysis evidenced higher structure retention in ribbon-like samples, whose fragmentation patterns (not shown) were similar to the one of bulk PTFE. This is in agreement with our findings by XPS, XRD, and FT-IR analyses, reported in previous papers [43,45]. Ribbon-like samples were found to be more ordered, partially crystalline, and fluorine-rich coatings.

Spatially resolved microbeam imaging was performed on structured samples, which allowed the study of fragment distribution over the entire sample surface. Image analysis was based on the observation that highly fluorinated fragments ($C_x F_y^+$, $y > x$) are indicative of PTFE-like composition, while C^+ ions suggest a more highly cross-linked, low-fluorine composition. In Fig. 9a, the C^+ ion distribution image is reported. When the individual highly fluorinated ions were considered, the corresponding image contrast was relatively poor. However, a composite image derived from the ratio of highly fluorinated ions to C^+ ions clearly shows a compositional variation between the ribbons and the substructure. This can be easily appreciated in Fig. 9b, which is the image of the parameter α_F, defined as:

$$\alpha_F = \frac{\sum I_{C_x F_y^+} (y > x)}{I_{C^+}} \tag{12}$$

where $I_{C_x F_y^+}$ is the SIMS intensity of the fluorinated fragments and I_{C^+} is that of C^+ ions. The images show that the ribbons are poor in C^+ and rich in highly fluorinated moieties with respect to the reminder of the sample, thus being more PTFE-like.
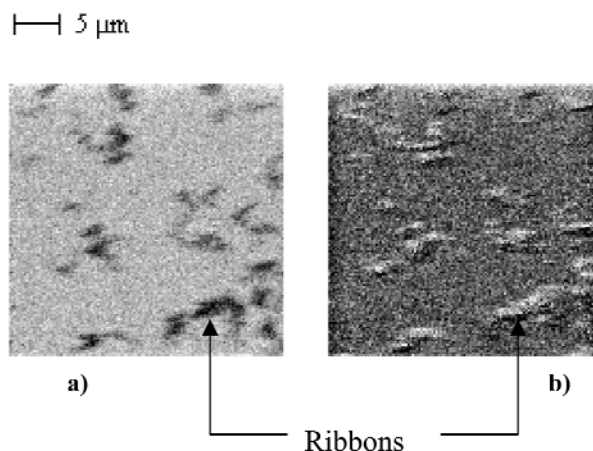

Fig. 9 ToF-SIMS images of (a) C^+ ion and of (b) the parameter α_F defined according to eq. 13.

DISCUSSION

On the basis of the results described for the compositional evolution of the plasma phase and for the structure and morphology of the deposited coatings, both in continuous and modulated regimes, the film deposition mechanism illustrated in Fig. 10 has been developed.

As previously described [43], at DC ≥ 10 % the depletion of monomer (reaction *a*), produces plenty of $\cdot CF_2$ radicals and modulated plasmas do not appear very different from continuous ones. When the density of radicals becomes high in the gas phase (high power, DC, and pressure), recombination reactions become significant, and lead to the formation of heavier fragments, $C_y F_z$, similar to

(a) $C_2F_{4\,(g)} + e \xrightarrow{k_D} 2\; {}^{\bullet}_{\bullet}CF_{2\,(g)} + e$

(b) ${}^{\bullet}_{\bullet}CF_{2\,(g)} \longrightarrow CF_x\,(x = 1\text{-}3)_{(g)} + F^{\bullet}_{(g)}$

(c) $Substrate + I^+, e \xrightarrow{k_{act}} Substrate*$

$$n\,CF_{x\,(g)} \xrightarrow[\substack{(d)}]{k_{rec}} C_yF_{z\,(g)} \xrightarrow[\substack{k^3_{pol} \\ (f)}]{k^g_{pol}} Powders$$

Substrate*

(g) $CF_{x\,(g)} + Substrate* \xrightarrow{k^1_{pol}} a\text{-}(CF_x)_{n\,(s)}$

(h) ${}^{\bullet}_{\bullet}CF_{2\,(g)} + Substrate* \rightleftharpoons {}^{\bullet}_{\bullet}CF_{2\,(ads)} \xrightarrow{k_{diff}} \xrightarrow{k^2_{pol}} nc\text{-}(CF_2)_{n\,(s)}$
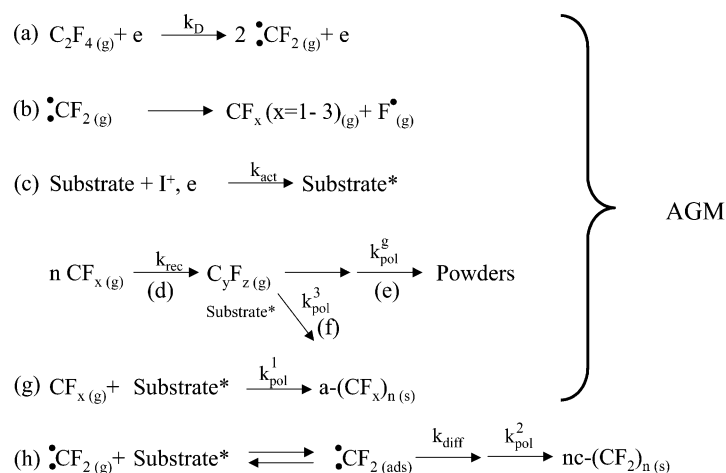
AGM

**Fig. 10** Scheme of the deposition mechanism developed for TFE continuous and modulated plasmas.

the saturated and unsaturated molecules identified by means of FT-IRAS (route *d*). This reaction path can also proceed, mainly at higher pressure, to form particulates (route *e*); however, this can be ruled out in the regimes leading to ribbon-like structures, as FT-IRAS absorption analysis does not reveal any formation of powders. It should be considered that besides ${}^{\bullet}_{\bullet}CF_2$, other small radicals, CF_x and $F^{\bullet}$ atoms, can also be produced (route *b*). However, these latter species and C_yF_z radicals, under low DC and input power, are likely formed to a much lesser extent, so that ${}^{\bullet}_{\bullet}CF_2$ remains the main film precursor. Reactions *g* and *h* represent two different film deposition pathways. In particular, reaction *g* refers to the high-rate formation of amorphous, flat and cross-linked films, $a\text{-}(CF_x)_n$, occurring at high DC and in continuous discharges according to the activated growth model of deposition (AGM) [30].

In the low ${}^{\bullet}_{\bullet}CF_2$ radical concentration regime (route *h*), that is, with DCs smaller than 10 %, the deposition rate and positive ion bombardment are drastically reduced and the few adsorbed ${}^{\bullet}_{\bullet}CF_2$ radicals have enough time to migrate on the surface to lower-energy sites, which become the nucleation centers for the formation of nanostructured crystalline PTFE-like ribbons, $nc\text{-}(CF_2)_n$.

According to the described mechanism, the changes in surface morphology seem to be mainly linked to:

- modulation itself, which provides an off time;
- migration of adsorbed radicals, mainly during this off time.

The cartoon shown in Fig. 11 is an attempt to explain the evolution of surface morphology with DC. Under the continuous deposition regime, the high and continuous flux of radicals and of ions ensures enough active sites for AGM, and many radicals readily to stick to these sites. Surface migration cannot occur, and only flat coatings are possible. At high pressure, the ${}^{\bullet}_{\bullet}CF_2$ and other small radical densities decrease, as found by actinometric optical emission spectroscopy (AOES) investigations [57], and heavier fragments (or even powders) are produced to a greater extent. The number of surface activated sites decreases, too, owing to reduced ion bombardment; thus, radicals have appreciably more time to diffuse across the surface toward energetically favorable sites, where they can aggregate resulting in a rougher surface. However, in this regime, it should be considered that heavier species, formed in the gas phase from association reactions of lighter species, and eventually powder granules, can contribute to film deposition (route *f*) and take part in the formation of the aggregates present on the film surface. A similar granular and rough morphology was described by Silverstein et al. for the plasma deposition of fluorocarbon films in continuous hexafluoropropylene (C_3F_6) plasmas at higher pressures (750–1500 mtorr). In this gas-phase driven plasma polymerization, submicrometer particles formed by homo-

CONTINUOUS MODE DEPOSITION

Radicals

Surface activated site

Flat amorphous coating
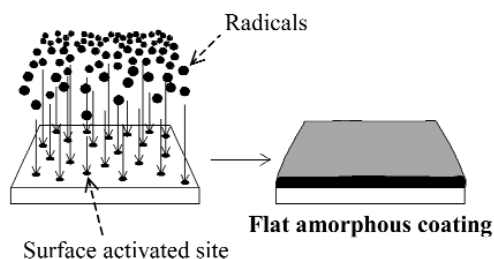
• High radicals concentration

• High surface activated sites concentration
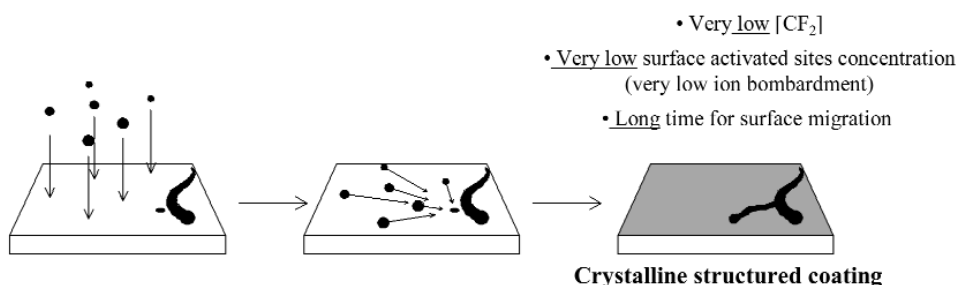(high ion bombardment; AGM is operative)

• Negligible surface migration

MODULATED DEPOSITION AT LOW DC AND HIGH PERIOD

• Very low [CF$_2$]

• Very low surface activated sites concentration
(very low ion bombardment)

• Long time for surface migration

Crystalline structured coating

MODULATED DEPOSITION AT HIGH DC AND HIGH PERIOD

• Medium [CF$_2$]

• Medium surface activated sites concentration
(medium ion bombardment)

• Medium time for surface migration

Bumpy Coating
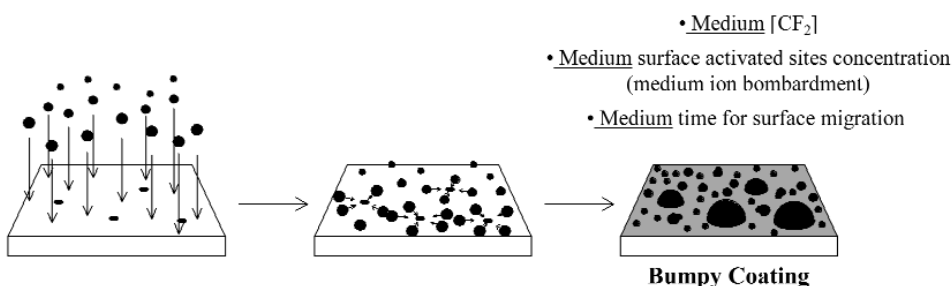
Fig. 11 Schematized deposition mechanism in different regimes.

geneous nucleation are believed to deposit on the surface, where they undergo further polymerization and become incorporated into the structure of the coating [58,59].

At 5 % DC and long period, the number of surface activated sites is low, as is the radical concentration in the plasma phase. Moreover, adsorbed radicals have more time (long off time) to migrate on the surface and to reach activated sites before the arrival of other impinging radicals (beginning of the on time). When a nucleation center is formed, it slowly grows for the preferential attachment of the other few incoming radicals, very likely $\cdot CF_2$. This leads to the formation of PTFE-like ribbons, whose direction of propagation depends primarily on the direction in which a greater concentration of nuclei is formed. When ribbons start to form, they can grow by both nuclei coalescence of and by direct attachment of radicals diffusing along the surface.

Linear rod-like aggregates consisting of extended chains with the chain axis parallel to the long axis of the rods were observed in thin films obtained from conventional PTFE [60] and in PTFE dispersions [61]. It was also reported that, at low polymerization rates, bulk PTFE polymerizes in chains

of helical conformation [62]. Thus, at low DC and long period, the deposition rate is low enough for the radicals to rearrange in ribbons, which appear to constitute a thermodynamically more stable form. However, when the DC is increased, the process becomes kinetically driven, and the anisotropy is progressively lost. The number of active sites on the sample surface increases, together with the radical concentration. As a consequence, the probability that each active site is reached by radicals coming from all possible directions increases, too, and this results in the formation of bumps over the entire surface, in particular for DCs higher than 20 %. Moreover, since the time for the radical migration decreases (shorter off time) and ion bombardment increases, the average heights of the nuclei as well as their height differences are lowered.

Surface morphologies similar to those obtained at high DCs in this work, have also been observed by Labelle et al. during the deposition of fluorocarbon films in modulated plasmas fed with HFPO, 1,1,2,2-tetrafluoroethane, and difluoromethane [63]. Lau et al. observed rod-like morphologies in addition to spherical grain ones, during hot filament chemical vapor deposition (HFCVD) of HFPO, and they speculated that the formation of spherical grains occurs at high deposition rate as a result of gas-phase nucleation, while rod-like arrangements prevail in a slow deposition regime, when chain growth is favored over gas-phase nucleation [14]. Ribbon-like structured coatings deposited from modulated discharges fed with other perfluoroalkane monomers were also reported by other authors [64]. Similarly, the ribbons develop under limited DC and input power conditions; moreover, evidence of the major role played by radical surface mobility in the occurrence of this unique morphology can be found therein.

At 5 % DC and decreased period, the $:CF_2$ concentration becomes higher, ion bombardment is progressively more effective, and the time left for radical diffusion is lower, which reduces both nuclei the formation of and growth. Going to lower periods (40 and 80 ms), only few aggregates (or none) are evidenced on a smooth grown film.

CONCLUSIONS

Continuous and modulated plasmas fed with TFE have been extensively investigated in this paper. In order to understand the general film deposition mechanism, both the plasma and film composition and structure were investigated. As the DC is increased in modulated discharges, monomer depletion also increases and many recombination reactions take place at progressively higher rates, leading to the formation of CF_4, C_2F_6, C_3F_6, C_3F_8, C_4F_{10}, as detected by FT-IRAS. No evidence of particulate formation was found under any working condition, thus ruling out a powder-promoted mechanism of deposition. The morphology of the deposited coatings is deeply influenced by the particular choice of experimental parameters, in particular by the modulation of the discharge. When switching from high DC and short period to low DC and long period, the coating passes from the commonly found flat, homogeneous, and amorphous structure, to ribbon-like structured films with a crystalline, PTFE-like nature. For intermediate values of DC and period, the coatings mainly consist of bumpy structures.

To account for the changes induced by the modulation parameters on the coating morphology, a mechanism based on the AGM has been proposed. The morphological features depend on the competition between surface migration of small adsorbed radicals towards nucleation centers, and their reaction with radicals impinging from the gas phase. If the DC and period are chosen in a suitable way, the adsorbed radicals have enough time to diffuse toward the nucleation centers and to form crystalline PTFE chains before being quenched by the impinging radicals.

ACKNOWLEDGMENT

REFERENCES

1. Web site: <http://www.omega.com/pdf/tubing/technical_section/teflon_flourocarbon.asp>.
2. J. P. S. Badyal, S. R. Coulson, R. C. Willis, S. A. Brewer. WO Patent 98/58117.
3. D. Kiaei, A. S. Hoffman, B. D. Ratner, T. A. Horbett. *J. Appl. Polym. Sci.: Polym. Symp.* **42**, 269 (1988).
4. D. Kiaei, A. S. Hoffman, T. A. Horbett. *J. Biomater. Sci. Polym. Ed.* **4**, 35 (1992).
5. P. Favia, V. H. Perez-Luna, T. Boland, D. G. Castner, B. D. Ratner. *Plasmas Polym.* **1**, 299 (1996).
6. G. Clarotti, F. Schue, J. Sledz, A. A. B. Aoumar, K. E. Geckler, A. Orsetti, G. Paleirac. *Biomaterials* **13**, 832 (1992).
7. J. L. Bohnert, B. C. Fowler, T. A. Horbett, A. S. Hoffman. *J. Biomater. Sci. Polym. Ed.* **1**, 279 (1990).
8. B. D. Ratner, A. Chilkoti, G. P. Lopez. In *Plasma Deposition, Treatment and Etching of Polymers*, R. d'Agostino (Ed.), Academic Press, New York (1990).
9. S. J. Limb, K. K. Gleason, D. J. Edell, E. F. Gleason. *J. Vac. Sci. Technol. A* **15**, 1814 (1997).
10. K. K. Gleason, S. J. H. Limb, E. F. Gleason, H. H. Sawin, D. J. Edell. U.S. patent 5,888,591.
11. C. C. Cho, D. M. Smith, J. Anderson. *Mater. Chem. Phys.* **42**, 91 (1995).
12. C. B. Labelle and K. K. Gleason. *J. Vac. Sci. Technol. A* **17**, 445 (1999).
13. K. K. S. Lau and K. K. Gleason. *Mater. Res. Soc. Symp. Proc.* **544**, 209 (1999).
14. K. K. S. Lau, J. A. Caulfield, K. K. Gleason. *Chem. Mater.* **12**, 3032 (2000).
15. K. K. S. Lau and K. K. Gleason. *J. Phys. Chem. B* **105**, 2303 (2001).
16. K. K. S. Lau, J. A. Caulfield, K. K. Gleason. *J. Vac. Sci. Technol. A* **18**, 2404 (2000).
17. F. Quaranta, A. Valentini, P. Favia, R. Lamendola, R. d'Agostino. *Appl. Phys. Lett.* **63**, 10 (1993).
18. J. L. He, W. Z. Li, L. D. Wang, J. Wang, H. D. Li. *Nucl. Instrum. Methods Phys. Res., Sect. B* **135**, 512 (1998).
19. T. C. Nason, J. A. Moore, T. M. Lu. *Appl. Phys. Lett.* **62**, 1866 (1992).
20. H. Usui, H. Koshikawa, K. Tanaka. *J. Vac. Sci. Technol. A* **13**, 2318 (1995).
21. G. B. Blanchet and S. I. Shah. *Appl. Phys. Lett.* **62**, 1026 (1993).
22. G. B. Blanchet, C. R. Fincher Jr., C. L. Jackson, S. I. Shah, K. H. Gardner. *Science* **262**, 719 (1993).
23. W. Jiang, M. G. Norton, L. Tsung, J. T. Dickinson. *J. Mater. Res.* **10**, 1038 (1995).
24. S. T. Li, E. Arenholz, J. Heitz, D. Bäuerle. *Appl. Surf. Sci.* **125**, 17 (1998).
25. R. Schwödiauer, J. Heitz, E. Arenholz, S. Bauer-Gogonea, S. Bauer, W. Wirges. *J. Polym. Sci., Part B: Polym. Phys.* **37**, 2115 (1999).
26. T. Katoh and Y. Zhang. *Appl. Phys. Lett.* **68**, 865 (1996).
27. T. Katoh and Y. Zhang. *Appl. Surf. Sci.* **138–139**, 165 (1999).
28. Y. Zhang, T. Katoh, A. Endo. *J. Phys. Chem. B* **104**, 6212 (2000).
29. S. J. Limb, C. B. Labelle, K. K. Gleason, D. J. Edell, E. F. Gleason. *Appl. Phys. Lett.* **68**, 2810 (1996).
30. R. d'Agostino, F. Cramarossa, F. Fracassi, F. Illuzzi. In *Plasma Deposition, Treatment and Etching of Polymers*, R. d'Agostino (Ed.), Academic Press, New York (1990).
31. V. Panchalingam, X. Chen, C. R. Savage, R. B. Timmons, R. C. Eberhart. *J. Appl. Polym. Sci.: Appl. Polym. Symp.* **54**, 123 (1994).
32. V. Panchalingam, B. Poon, H. H. Huo, C. R. Savage, R. B. Timmons, R. C. Eberhart. *J. Biomater. Sci. Polym. Ed.* **5**, 131 (1993).
33. S. J. Limb, K. K. S. Lau, D. J. Edell, E. F. Gleason, K. K. Gleason. *Plasmas Polym.* **4**, 21 (1999).
34. S. R. Coulson, I. S. Woodward, J. P. S. Badyal, S. A. Brewer, C. Willis. *Langmuir* **16**, 6287 (2000).
35. S. J. Limb, D. J. Edell, E. F. Gleason, K. K. Gleason. *J. Appl. Polym. Sci.* **67**, 1489 (1998).
36. C. R. Savage, R. B. Timmons, J. W. Lin. *Chem. Mater.* **3**, 575 (1991).

37. C. I. Butoi, N. M. Mackie, L. J. Gamble, D. G. Castner, J. Barnd, A. M. Miller, E. R. Fisher. *Chem. Mater.* **12**, 2014 (2000).
38. B. D. Washo. *Org. Coat. Appl. Polym. Sci. (Am. Chem. Soc.)* **47**, 69 (1982).
39. M. Morra, E. Occhiello, F. Garbassi. *Langmuir* **5**, 872 (1989).
40. S. R. Coulson, I. Woodward, J. P. S. Badyal, S. A. Brewer, C. Willis. *J. Phys. Chem. B* **104**, 8836 (2000).
41. J. P. Yongblood and T. J. McCarthy. *Macromolecules* **32**, 6800 (1999).
42. R. N. Wenzel. *J. Phys. Colloid Chem.* **53**, 1466 (1949).
43. G. Cicala, A. Milella, F. Palumbo, P. Rossini, P. Favia, R. d'Agostino. *Macromolecules* **35**, 8920 (2002).
44. G. Cicala, A. Milella, F. Palumbo, P. Favia, R. d'Agostino. *Diamond Relat. Mater.* **12**, 2020 (2003).
45. P. Favia, G. Cicala, A. Milella, F. Palumbo, P. Rossini, R. d'Agostino. *Surf. Coat. Technol.* **169–170**, 609 (2003).
46. M. Creatore, F. Palumbo, R. d'Agostino. *Pure Appl. Chem.* **74**, 407 (2002).
47. B. A. Cruden, M. V. V. S. Rao, S. P. Sharma, M. Meyyappan. *Plasma Sources Sci. Technol.* **11**, 77 (2002).
48. Bruker Equinox 55 Reference Manual.
49. M. Haverlag. Ph.D. thesis, Eindhoven University of Technology (1991).
50. A. M. Hynes, M. J. Shenton, J. P. S. Badyal. *Macromolecules* **29**, 18 (1996).
51. A. M. Hynes, M. J. Shenton, J. P. S. Badyal. *Macromolecules* **29**, 4220 (1996).
52. T. Shirafuji, Y. Nakagami, Y. Hayashi, S. Nishino. *Jpn. J. Appl. Phys.* **38**, 4520 (1999).
53. F. W. Breitbarth, D. Berg, K. Dumke, H. J. Tiller. *Plasma Chem. Plasma Process.* **17**, 39 (1997).
54. E. Stoffels and W. W. Stoffels. Ph.D. thesis, Eindhoven University of Technology (1994).
55. W. W. Stoffels, E. Stoffels, G. Kroesen, M. Haverlag, J. den Boer, F. Hoog. *Plasma Sources Sci. Technol.* **3**, 320 (1994).
56. P. R. i Cabarrocas, A. F. i Morral, S. Lebib, Y. Poissant. *Pure Appl. Chem.* **74**, 359 (2002).
57. A. Milella. Ph.D. thesis, University of Bari (2002).
58. R. Chen and M. S. Silverstein. *J. Polym. Sci., Part A: Polym. Chem.* **34**, 207 (1996).
59. R. Chen, V. Gorelik, M. S. Silverstein. *J. Appl. Polym. Sci.* **56**, 615 (1995).
60. T. Hashimoto, Y. Murakami, H. Kawai. *J. Polym. Sci., Polym. Phys. Ed.* **13**, 1613 (1975).
61. H. D. Chanzy, P. Smith, J. F. Revol. *J. Polym. Sci., Polym. Lett. Ed.* **24**, 557 (1986).
62. C. W. Bunn and E. R. Howells. *Nature* **174**, 549 (1954).
63. C. B. Labelle and K. K. Gleason. *J. Appl. Polym. Sci.* **74**, 2439 (1999).
64. H. Qui. Ph.D. thesis, The University of Texas at Arlington (2001).